Pristine Carbon Nanotubes are Efficient Absorbers at Radio Frequencies

Nicholas J. Rommelfanger^{1,4}, Kenneth Brinson Jr^{2,4}, John E. Bailey^{2,3,4}, Analiese M. Bancroft^{2,4}, Zihao Ou^{2,4}, and Guosong Hong^{2,4,*}

- ¹ Department of Applied Physics, Stanford University, Stanford, CA, 94305, USA
- ² Department of Materials Science and Engineering, Stanford University, Stanford, CA, 94305, USA
- ³ Department of Electrical Engineering, Stanford University, Stanford, CA, 94305, USA
- ⁴ Wu Tsai Neurosciences Institute, Stanford University, Stanford, CA, 94305, USA
- * Corresponding author: guosongh@stanford.edu

Abstract

Radio frequency ablation and microwave hyperthermia are powerful tools for destroying dysfunctional biological tissues. However, wireless application of these techniques is hindered by their inability to focus the electromagnetic energy to small targets. The use of locally injected radio frequency- or microwave-absorbing nanomaterials can help to overcome this challenge by confining heat production to the injected region. Previous theoretical work suggests that highaspect-ratio conducting nanomaterials, such as carbon nanotubes, offer powerful radio frequency and microwave absorption. While carbon nanotubes have been demonstrated as radiothermal agents, common solubilization methods may reduce their absorption efficiency, yielding undesirable nonspecific heating in the biological tissue background. In this manuscript, we hypothesize that pristine carbon nanotubes can act as efficient absorbers at radio frequencies, thus providing differential heating over the tissue background. Specifically, we use a sonicationfree preparation technique to preserve both the high aspect ratio and local concentration of pristine carbon nanotubes. We validate the differential heating of these samples by 4.5-fold at 2 GHz compared to the heating of saline at a physiological concentration using infrared thermography. In addition, we successfully achieved local heating of pristine carbon nanotubes within a three-dimensional biological tissue phantom. Numerical simulations further aid in producing a temperature map within the phantom and confirming localized heating. Due to their significant differential and local heating, we believe that pristine carbon nanotubes may facilitate region-specific radio frequency ablation and microwave hyperthermia while keeping nonspecific heating to a low level in the normal tissue background.

Keywords: Differential heating, local heating, region specificity, microwave, relative absorption ratio, radiothermal, cancer

1. Introduction

Radio frequency ablation (RFA) and microwave hyperthermia (MH) enable cancer treatment and the correction of electrical conduction abnormalities in the heart [1,2]. The therapeutic efficacy of these techniques relies on the selective destruction of aberrant tissue by concentrating the electric field and subsequently heating the target tissue. With spatially confined differential heating, this approach produces a local temperature increase sufficient to destroy the target tissue while sparing the surrounding tissues. However, unlike photothermal therapy that wirelessly focuses

visible light to produce differential heating on the microscale in biological tissues, RFA and MH usually require an implanted antenna to focus energy to mm-cm sized tissue targets. This requirement of invasive implantation arises from the MHz to GHz frequencies associated with RFA and MH, which prevent useful focusing of far-field radiation to sub-diffraction sizes. The diffraction limit requires that antennas optimized for near-field heating must be employed instead of far-field focusing. These near-field antennas require close contact with the target tissue, often involving an invasive procedure to implant the antennas or surgically remove overlying tissues [1].

Alternatively, injected materials with enhanced absorption of radio frequency (RF) and microwave fields represent a wireless approach for focused RFA and MH. Our recent theoretical work based on the electrostatic approximation suggested that high-aspect-ratio, conductive metal nanowires are promising "nanoantennas" to produce differential heating under RF irradiation from MHz to GHz frequencies [3,4]. Owing to their sub-wavelength sizes, these nanoantennas may break the diffraction limit to effectively focus RF absorption to areas and volumes much smaller than the RF wavelength. This theoretical work suggests that conductive high-aspect-ratio nanostructures, such as single-walled carbon nanotubes (CNTs), may serve as effective nanoantennas, thus producing localized differential heating in RF-irradiated biological tissue.

CNTs are long ropes of covalently bonded carbon atoms with high conductivities that enable their use as transparent electrodes in flexible electronics [5]. Depending on their synthesis and separation technique, single-walled CNTs can achieve an extremely high aspect ratio up to >10⁷ [6] with a high conductivity up to 10⁶ S cm⁻¹ [7]. These unique properties of CNTs thus make them promising candidates of RF nanoantennas for achieving differential heating in biological tissues. Previous publications have put forth theoretical models to describe RF interactions with CNTs to produce heating and local field enhancement [8]. Additionally, several studies attempted to experimentally validate the utility of CNTs for RFA and MH [9–11]. Despite these reports, a significant challenge of applying CNTs for RFA and MH *in vivo* arises from nonspecific RF absorption by soft tissue, especially that by the water molecules and ions therein. As a result, it remains challenging to produce significant differential heating with CNTs while minimizing the nonspecific thermal effect of radio frequencies in the tissue background.

To mitigate this challenge, we argue that there are at least two missed opportunities of using CNTs as RF absorbers. First, our recent theoretical framework predicts greater absorption of RF energy by an antenna with a higher aspect ratio [3]. Second, the Fourier heat equation prescribes that significant local heating in the biological tissue can only be achieved with a high local concentration of antennas with nanometer sizes [12]. Therefore, we hypothesize that maximum RF absorption can be achieved in as-grown CNTs with minimal post-processing (e.g., sonication), thus preserving their original lengths, pristine conductivity, and high local concentration. To validate this hypothesis, we leveraged the small diameter (ca. 1 nm) and unreduced lengths (>1 µm) of pristine CNTs synthesized via the high-pressure carbon monoxide conversion (HiPCO) method to maximize the aspect ratio as advised by the theoretical models. We proved our hypothesis by demonstrating significantly greater RF absorption by pristine CNTs than their sonicated and functionalized counterparts at the same mass concentration. Using pristine CNTs

at an achievable concentration, we observed their significant differential heating compared to saline at a physiological concentration under 2-GHz RF irradiation, thus confirming their efficient absorption of RF energy. Infrared thermography and numerical simulations revealed spatially confined differential heating of pristine CNTs inside a tissue phantom with a comparable dielectric function to that of muscle upon exposure to incident RF energy. Our findings suggest the potential of using pristine CNTs as nanoantennas to "focus" RF energy for applications that require localized tissue heating via wireless means.

2. Methods

2.1. Sample preparation

To prepare sonicated CNT suspensions for comparison to pristine CNT suspensions at the same concentration (0.5 mg/mL), 2 mg of HiPCO CNTs were added to 4 mL of deionized (DI) water in a 10 mL glass scintillation vial. 20 mg/mL of sodium deoxycholate was also added to aid with CNT suspension. This mixture was then placed in an ice bath (to prevent overheating) and sonicated using a Qsonica CL-18 tip sonicator at 60 W for 1 h (continuous wave). Capillary tubes (20 mm long, 1.2 mm inner diameter, 1.6-1.8 mm outer diameter, Kimble 34500) were filled with the sonicated CNT solution via capillary action. To prepare an unsonicated, pristine CNT sample for comparison, 2 mg of HiPCO CNTs were added to 4 mL of deionized (DI) water in a 10 mL glass scintillation vial with 20 mg/mL of sodium deoxycholate. To ensure the pristine CNT sample was mixed as thoroughly as possible without applying the damaging force of sonication, the mixture was mechanically stirred with a magnetic stir bar rotating at 1500 revolutions per minute for 1 h. Capillary tubes were filled using capillary action while the mixture was under active stirring to aid in collecting the same concentration of CNTs as for the sonicated case. To control for the heating effects of the surfactant, a separate 20 mg/mL solution of sodium deoxycholate in DI water was also prepared. The ends of all capillary tubes were sealed with superglue (Loctite 495) to prevent evaporation during testing.

To prepare high-concentration pristine CNT suspensions in PBS, 2.5 mg of HiPCO CNTs were added to a 2 mL centrifuge tube (Fisher Scientific) with 1 mL phosphate buffered saline (PBS, 1X) (Gibco). The centrifuge tube was inverted by hand several times to wet the CNTs with PBS, but no additional mixing was performed, and no surfactant was added. This mixture was centrifuged at 4,000 g for 15 minutes to discard the PBS supernatant that did not suspend any CNTs. Capillary tubes were filled with the CNT suspension by repeatedly pressing the tubes into the suspension in the centrifuge tube. For control experiments with the same background fluid, PBS was drawn directly into capillary tubes. The ends of all capillary tubes were sealed with superglue after filling to prevent evaporation during testing. By weighing the contents within CNT-filled capillary tubes and comparing to the mass measured after heating on a hot plate (220°C) for 1 h (allowing for full evaporation of water), it was found that this loading technique yielded high CNT mass fractions of $\sim 3.1\% \pm 0.9\%$ (mean \pm standard deviation), equivalent to a CNT concentration of $\sim 32 \pm 10$ mg/mL. The remainder of the mass was PBS 1X.

Hemispherical PBS hydrogels were created by mixing agarose (Lonza SeaPlaque) with PBS at a concentration of 12.5 mg/mL. The mixture was heated in an oven at 70°C for 30 minutes before being poured into a three-dimensional (3D)-printed hemispherical mold with 2 cm diameter. The hydrogel was refrigerated at 4°C for ~15 minutes until it solidified, at which time it was removed from the mold with a spoon. Control experiments used this hemispherical hydrogel directly. For CNT experiments, a cylindrical void was cored from the hydrogel (centered ~2.6 mm behind the face) by inserting and then removing an empty capillary tube. Next, a capillary tube filled with a high-concentration suspension of CNTs (see procedure in previous paragraph) was pushed into the cylindrical void, and the CNTs were forced out of the capillary tube via a 3D-printed "plunger". The space above this CNT "injection" was then replaced with previously cored hydrogel to seal the CNTs into the hydrogel hemisphere.

2.2. Sample characterization

A Thermo Fisher Scientific Apreo S LoVac scanning electron microscope (SEM) was used to image the CNTs with a 5kV imaging voltage and 0.1 nA current. For scanning electron microscopy, CNTs deposited from a slurry in toluene were imaged directly without additional preparation to mimic the sonication-free samples used in experiments. A Thermo Fisher Scientific Evolution 350 UV-Vis spectrophotometer was used to measure the absorption spectrum of CNTs solubilized in an aqueous solution. Specifically, 0.25 mg/mL CNTs were dispersed in deionized water with 10 mg/mL sodium deoxycholate using probe sonication (Fisherbrand Model 120 generator with Qsonica CL-18 probe) at 100 Watts for 6 minutes (3-s pulses at 50% duty cycle), yielding a well-dispersed CNT suspension. The absorption spectrum was smoothed using a moving-average filter 5 data points wide (one data point per nanometer). The derivative was taken from the smoothed spectrum in the increasing-wavelength direction, and the derivative spectrum was smoothed again in the same way [13]. The absorption peaks of metallic and semiconducting CNTs differ, thus enabling UV-visible spectroscopy measurements of the metallic vs. semiconducting CNT ratio within a sample. Huang et al. report that the fraction of metallic CNTs in a sample is given by $(1 + f S_{22} / M_{11})^{-1}$, where the absorption coefficient f = 1.05 is reported for HiPCO CNTs, and S₂₂ and M₁₁ are measured peak heights of the S₂₂ and M₁₁ regions [14]. For HiPCO CNTs, M₁₁ is reported to span from 470 nm - 650 nm, and S₂₂ is reported to span from 580 nm - 920 nm. The absorbance spectrum of the CNTs used in this work is plotted in figure 1(c), along with the derivative of the absorbance. Following reported techniques, peak heights were measured from the derivative of absorbance to minimize the effects of the background [13]. The heights of the peaks falling within the M₁₁ and S₂₂ regions (marked with black bars) were summed. The peak at 595 nm fell in the region where M₁₁ and S₂₂ overlap, so the peak was thus alternately assigned to M_{11} and S_{22} to determine the bounds on the metallic CNT fraction. A Horiba XploRA Plus was used to collect the Raman spectrum of pristine CNTs. The pristine CNT suspension was drop cast on a silicon wafer and dried in a desiccator. A 785 nm laser was used to collect the Raman spectrum, with an acquisition time of 5 s and 10 accumulations.

2.3. Radio-frequency heating experiments

RF signals at 2 GHz were produced by a Berkeley Nucleonics Model 845 generator and were amplified by an Amplifier Research 200T1G3A power amplifier. The amplified signal was inserted into a broadband transverse electromagnetic (TEM) cell (TekBox TBTC0), with 135 ± 1 Watts delivered to the TEM cell for capillary tube experiments of sonicated vs. pristine CNT samples (data presented in figure 2) and with 45 ± 1 Watts delivered to the TEM cell for high-concentration pristine CNT experiments and for hydrogel experiments (data presented in figures 3, 4, S1, and S2). Additional power was needed to produce heating for the sonicated vs. pristine CNT comparison due to a lower concentration of CNTs and ions in these samples. The TEM cell was terminated at 50 Ohms (Bird 8201 Termaline) to minimize reflected power. Pairs of capillary tubes were vertically affixed via double-sided tape to opposite sides of a 3D-printed sample holder (polylactic acid, Ender-3 printer, figure S3) placed in the center of the TEM cell. In this orientation, the long axis of the capillary tubes was aligned with the direction of the electric field within the TEM cell. The electric field strength within the TEM cell varied slightly with position, so for each pair of capillary tubes, 5 trials were conducted with the tubes on either side of the sample holder, in order to ensure equal field exposure between the two tubes over their set of 10 total trials. Four unique capillary tubes were produced for each sample, making for 40 total trials for each sample. For hydrogel experiments, the hemispherical hydrogel was held upright by a 3D-printed sample holder, with a strip of tape supporting the rounded side of the hemisphere (figure S4). The sample holder was fixed in the same position in the TEM cell for the control and CNT hydrogel experiments. For all experiments, temperature was monitored using a FLIR A325sc thermal camera.

2.4. Data analysis

For capillary tube heating experiments, the mean temperature vs. time of each tube was extracted by averaging over a fixed rectangular box placed over the capillary tube in the FLIR ResearchIR software. The change in temperature, ΔT , was calculated based on the increase of the mean capillary tube temperature since t=0 when the RF power was initiated. For hydrogel heating experiments, the mean temperature vs. time on the surface of each hydrogel was extracted by averaging over a circular region of interest (ROI) centered on the hydrogel in MATLAB (ROI shown in figure S1 for all samples). This circular ROI had a diameter of 5 mm, compared to the 2 cm diameter of the hydrogel itself. For all statistical analyses comparing ΔT after RF heating, two-tailed unpaired t-tests were used to determine significance.

2.5. Finite Element Method (FEM)

FEM simulations were conducted in COMSOL Multiphysics 5.6. Dielectric and thermal parameters used for pure PBS and the suspension of pristine CNTs in PBS are given in Table 1. PBS was assigned the thermal properties of water, and the dielectric function of PBS at 2 GHz is reported in the literature [15]. The density of the pristine CNT suspension in PBS is the average density of four samples measured during the experiments. The specific heat of the pristine CNT suspension is a weighted average based on the average CNT vs. water mass fractions (3.1% CNTs, 96.9% water, described in section 2.1), where the specific heat for single-walled CNTs is

reported in the literature as ~640 J/(kg K) at room temperature [16]. The thermal conductivity of the pristine CNT suspension was taken to equal that of water, the samples' largest constituent.

A PBS hemisphere with a diameter of 2 cm was oriented with its face pointed into the wave's propagation direction, as in experiments. The hemisphere was suspended in the center of the simulation domain, and an "external natural convection" boundary was set on its surface (assuming a spherical geometry with 2 cm diameter, surrounded by 22°C air at 1 atm). The initial temperature for the hemisphere was fixed at 18°C to match experiments, as the hydrogel was stored in the refrigerator to prevent melting and evaporation.

A RF wave (TE₁₀ mode) was coupled into a 30 cm by 20 cm rectangular waveguide port with "perfect electrical conductor" boundary conditions. RF power was applied for 20 s. For control simulations, the magnitude of the RF power coupled into the waveguide was tuned until the mean ΔT within the circular ROI on the face of the hemisphere (described in Section 2.4) matched the mean ΔT in the same ROI from control experiments (averaged over n = 6) after 20 s of heating. This tuning process yields an input RF power of 178 W for simulations. The input RF power was then fixed at this magnitude for all control and CNT simulations presented in figure 4. Because the exact dielectric function of the CNT mixture was unknown, a cylindrical heat source (1.8 mm diameter, 9.5 mm length, matching the average injection geometry from experiments in Table S1) was added inside the PBS hemisphere, centered 2.6 mm behind the face of the hemisphere (average injection depth from Table S1). This cylinder had the thermal properties listed in Table 1 for the CNT suspension, but its dielectric function was set to match PBS so that the original background heating of the hemisphere was unaffected. This additional heat source due to CNT absorption of RF irradiation was applied concurrently with the RF power for 20 s. The magnitude of the additional heat source was tuned until the mean ΔT within the circular ROI on the face of the hemisphere (described in Section 2.4) matched the mean ΔT in the same ROI from the CNT experiments (averaged over n = 6) after 20 s of heating (resulting in 6 MW/m³ heat source). Once the magnitude of the input RF power and the additional heat source were fixed based on experimental results, the temperature of the interior of the hemisphere was measured at 2.6 mm depth (the center of the injection) for both control and CNT simulations. The average ΔT of the cylindrical injection ROI (1.8 mm diameter, 9.5 mm length) and the average power dissipation within this cylinder were also extracted for both control and CNT simulations.

To approximately extrapolate results for the six control and six CNT hydrogels in experiments, we use the fact that the simulation results were produced from the average ΔT and average injection dimensions measured from the control and CNT samples. Thus, for each control hydrogel sample, we take the ratio of the sample's surface ΔT to that of the mean surface ΔT of the six hydrogel samples. We then multiply the extracted mean ΔT in the cylindrical ROI (1.8°C) and the extracted power density (0.36 MW/m³) in the cylindrical ROI by this ratio. We follow the same protocol for the CNT hydrogels. The results are plotted in figure 4(n) and 4(o), respectively, where we extrapolate significant increases in temperature and dissipated power for the CNT hydrogels compared to the control hydrogels.

For all simulations, a free tetrahedral mesh was used to mesh the domain, adjusted to increase its resolution near the hydrogel sphere and the cylindrical injection within. Multiple simulations were conducted with different characteristic mesh sizes to ensure that increasing the resolution of the mesh had minimal effect on the output.

3. Results and Discussion

We hypothesized that pristine CNTs offer maximum RF absorption and heating due to the preservation of their original lengths, conductivity, and concentration, thus yielding maximum differential and local heating over nonspecific RF absorption and heating by soft tissue. Therefore, pristine CNTs should act as ideal "radiothermal" agents for hyperthermia treatments with high region specificity and minimal nonspecific heating in the tissue background (figure 1(a)). We first validated the high aspect ratio of pristine CNTs with SEM imaging. The SEM image in figure 1(b) reveals the exceptional lengths of pristine HiPCO CNTs used in this work, which formed bundles with >10 µm lengths in a tangled network. It has been reported that sonication of CNTs with surfactants, a common method to solubilize CNTs in water, severs CNTs into shorter pieces with lengths of <1 µm [17]. Our recent paper theoretically predicted that conductive nanowires with a high aspect ratio are efficient RF absorbers to produce differential heating over nonspecific tissue heating [3]. Combined with the nanometer diameter of HiPCO CNTs (0.8~1.2 nm), the preserved lengths of pristine CNTs yield an extraordinary aspect ratio that favors RF absorption and differential heating in tissues, thus potentially making these pristine CNTs efficient RF "nanoantennas".

We next sought to measure the percentage of metallic CNTs in the HiPCO mixture, since metallic CNTs with higher conductivity than their semiconducting counterparts are preferred as radiothermal agents. Using a reported approach based on the UV-Vis-NIR absorption spectrum of CNTs (figure 1(c)), we found a metallic fraction of 31~46% for the HiPCO CNT sample. Lastly, we performed Raman spectroscopy on the pristine CNT sample to confirm the presence of characteristic CNT bands. Indeed, in figure 1(d) we observe the D, G-, G+, and M bands that are indicative of CNTs [18].

Having demonstrated the high aspect ratio and metallic percentage of pristine HiPCO CNTs, we then performed experiments to validate their superior RF absorption and heating over saline and tissue phantoms with a physiological concentration of electrolytes. These experiments are necessary to demonstrate the unique capability of pristine CNTs to produce local differential heating while minimizing nonspecific RF absorption of the biological tissue background, thus proving our theory-guided hypothesis. Specifically, the frequency of 2 GHz was selected to measure the heating capabilities of the CNTs, as it falls near multiple industrial, scientific, and medical (ISM) bands used for hyperthermia treatments at 915 MHz and 2.45 GHz [19], as well as offering a minimum in reflected power with the RF equipment used for testing.

We first aimed to experimentally verify that although CNTs have been found to absorb RF and heat in previous reports, CNT suspensions conventionally produced by sonication cannot yield

significant differential heating over the aqueous background. We hypothesized that the RF absorption of CNTs is significantly reduced after sonication, and suspensions made of unprocessed pristine CNTs are more desirable RF absorbers for RFA and MH in vivo. To confirm this hypothesis, we compared the RF heating of suspensions of sonicated and pristine CNTs at the same concentration of 0.5 mg/mL in DI water. Sodium deoxycholate (20 mg/mL) was added to both samples to assist with suspension. Sonication is well known to solubilize CNTs in a stable suspension while shortening their lengths [20]. We demonstrate the superior heating of pristine CNTs compared to sonicated CNTs in figure 2. Representative thermal images of capillary tubes containing pristine vs. sonicated CNTs in figures 2(a)-2(c) show a significantly higher temperature increase for the pristine suspension, with their time traces of temperature increases summarized in figure 2(d). A statistical analysis comparing the average increase in temperature after 10 s is shown in figure 2(e), comparing pristine and sonicated samples to controls consisting of 20 mg/mL sodium deoxycholate in DI water. While the sonicated CNT samples at a concentration of 0.5 mg/mL do offer a slight increase in heating over the control samples of surfactant alone, a statistically significant increase in temperature is produced with pristine CNTs, thus suggesting the superior absorption of RF energy by the latter. This contrast in the heating of sonicated and pristine CNT suspensions demonstrates the importance of maintaining the length of CNTs for RF heating applications, thereby confirming the theoretical prediction [3] and proving our hypothesis.

Having demonstrated more-efficient RF absorption and heating by pristine CNTs, we next sought to maximize the concentration of pristine CNTs (see Section 2.1). For these experiments, PBS 1X was selected as a control solution due to its comparable dielectric function to that of biological tissue at 2 GHz and our ultimate goal of maximizing local differential heating of RF absorbers over the tissue background. For reference, the dielectric function of PBS 1X at 2 GHz was measured as 78.4 + 26.7i [15], sufficiently close to that of human paravertebral muscle, which was measured in vivo as 58 + 19i [21]. The applied RF power for experiments with PBS controls was reduced to demonstrate the minimization of nonspecific tissue heating necessary for efficacious in vivo experiments. Figures 3(a), 3(b), and 3(c) demonstrate the differential heating capabilities of the pristine suspension of CNTs in PBS vs. pure PBS under RF irradiation via thermal imaging. The average temperature rise of the capillary tube filled with PBS is moderate over 3 s of heating, increasing by <1°C over this time (time trace plotted in figure 3(d)). In contrast, the capillary tube filled with the pristine CNT suspension heats rapidly under the RF irradiation, with its average temperature increasing by over 4°C within the same 3-s period. A statistical analysis of the temperature increase over the first 3 s between PBS- and CNT-filled capillary tubes shows a significant increase in heating for CNT samples, with an average heating rate of 1.5°C/s for CNTs over the first 3 s of heating (figure 3(e)).

Having proven significant differential heating of pristine CNTs over a PBS solution with similar electrolyte concentrations as soft tissue, we next demonstrated local heating of pristine CNTs in a biological tissue phantom made of a PBS hydrogel. A 2-cm diameter hydrogel sphere comprising 1X PBS was placed inside of the TEM cell for RF irradiation. However, the heating rate of a CNT "injection" into the center of the spherical hydrogel was difficult to measure with a thermal camera due to the significant thermal diffusion before the heat reaches the surface of the hydrogel. This thermal diffusion masks the difference in surface temperature detected by the

thermal camera. Thus, the spherical hydrogel was instead cut into a hemisphere to improve the quality of the signal recorded during thermal imaging.

A photograph of a representative control hemispherical hydrogel is shown in figure 4(a), held upright by a 3D-printed rack within the TEM cell. Thermal images of this representative hydrogel under RF irradiation are shown in figures 4(b), 4(c), and 4(d). The hydrogel's initial temperature is approximately 18°C due to storage in the refrigerator (room temperature was ~22°C), and heating of the hydrogel's surface up to ~21.7°C is observed after 20 s of RF irradiation. Thermal images from experiments with five additional control hydrogels are presented in figure S2(a-e). FEM simulations were conducted in COMSOL Multiphysics to model the RF heating of a control hydrogel. The use of FEM simulations is helpful to quantify the 3D temperature distribution within the tissue phantoms, which is difficult to measure experimentally at high resolution in three dimensions. Following the procedure described in section 2.5, we produce the temperature map in figure 4(e) of the hydrogel surface after 20 s of heating, which approximately matches the representative temperature map shown in figure 4(d).

Next, pristine CNTs were injected 2.6 mm behind the face of hemispherical hydrogels, with a representative photograph of a hydrogel within the TEM cell in figure 4(g). The same RF power and duration as used for the control hydrogels was applied to the CNT hydrogels, and thermal images of a representative CNT-injected hydrogel are shown in figures 4(h), 4(i), and 4(j). As for the control hydrogel, the initial temperature of the CNT hydrogel was around 18°C. After 20 s of RF heating, the temperature of the representative hydrogel surface in front of the CNT injection had risen to ~23°C. A comparison of figures 4(d) and 4(j) suggests that an enhancement in heating is indeed offered at the site of a CNT injection. Thermal images from experiments with five additional CNT hydrogels are presented in figure S2(f-j). The statistical analysis in figure 4(m) comparing the mean surface temperature within the circular ROIs marked in figure S1 shows that CNT injections produce a significant improvement in heating on the surface of the hydrogel.

Building on this result, FEM simulations are capable of better quantifying the magnitude of this enhancement in heating, which arises from pristine CNTs injected into the hydrogels. As a result of the interior location of this heating source, the temperature increase at the depth of injection is expected to be greater than that on the surface due to thermal diffusion. Following the procedure described in section 2.5, the case of a CNT-injected hydrogel is simulated, yielding the surface temperature map shown in figure 4(k), which approximately matches the representative surface temperature map in figure 4(j). Now with 3D simulation results that have been tuned to match experiments for both the control and CNT hydrogels, the interior temperature of each hydrogel can be quantified. The increase in temperature on the plane located 2.6 mm behind the face of the hemisphere (that is, the plane of the CNT injection) is plotted for the control and CNT hydrogels in figures 4(f) and 4(l), respectively. The heating improvement offered by CNTs within the tissue is evident from a comparison of these two-dimensional temperature maps. Additionally, we extrapolated the average ΔT and power dissipation within the cylindrical volume for both control and CNT-injected hydrogel samples. The extrapolation was conducted by matching the simulation results to the experimentally measured surface ΔT from both control and CNT-injected hydrogel samples (see methods in Section 2.5). Specifically, we found an average ΔT of 6.8°C

within the cylindrical volume for CNT-injected hydrogels, significantly higher than that of 1.8°C for control hydrogels (figure 4(n)). In addition, CNTs injected into the hydrogel exhibited much higher RF absorption than hydrogel alone, as evidenced by an average heating power of 6.36 MW/m³ for the CNT hydrogel and only 0.36 MW/m³ for the control hydrogel (figure 4(o)). This analysis, though approximate in nature, provides a guideline for error estimation in measuring temperature distribution within the hydrogel, since the surface temperature should be proportional to both internal temperature and internal power dissipation.

The results presented here represent a significant advance for CNT-mediated RF hyperthermia. Although RF heating of CNTs has been reported previously [8–11], a significant challenge of applying CNTs for radiofrequency ablation *in vivo* arises from nonspecific RF absorption by water and ions in soft tissue. It is thus challenging to produce local differential heating with CNTs while minimizing nonspecific heating in the tissue background. In contrast, our results demonstrate significant local and differential heating afforded by pristine CNTs, owing to their preserved lengths and high concentrations after minimal processing. These results are guided by our recent theory, which predicts that a greater length and thus a higher aspect ratio of CNTs yields higher RF absorption. Our study experimentally validated these theoretical predictions with pristine CNTs to achieve maximum differential and local heating over PBS and a tissue phantom, which has never been accomplished in previous reports.

Specifically, we highlight the main differences between previous reports and our work as follows. First, several previous works compared the heating of CNTs only to a reference sample of DI water [9], while a comparison to a saline solution or a tissue phantom with realistic dielectric function is needed to demonstrate differential heating over the biological tissue background. Second, previous work with sonicated CNTs revealed only a 27% increase in heating compared to PBS even at an incident power of 900 W [10], a power that was later shown to be lethal to mice [11]. In contrast, our work demonstrates a 4.5-fold increase in differential heating using pristine CNTs over PBS with 20 times less power (figure 3). Third, owing to the significant differential heating of pristine CNTs over PBS, this paper presents the first clear evidence of spatially localized heating via temperature mapping and modeling (figure 4). This evidence indicates the ability of pristine CNTs to concentrate incident RF energy while sparing the surrounding tissue background, thus representing a necessary step for *in vivo* hyperthermia applications. In contrast, some recent work of MH, albeit efficacious, has missed the opportunity to provide the evidence of a localized temperature increase for hyperthermia experiments *in vivo* [11].

We believe that our results bring new insight to the optimization of efficient absorbers for RF hyperthermia by preserving the lengths and concentrations of pristine CNTs in a suspension. Pristine CNTs strongly contrast with conventional CNT suspensions reported for RF hyperthermia enhancement, the latter of which require sonication to disperse and functionalize CNTs, thus reducing their lengths and RF absorption. This novel approach shows promise for use in applications that require region-specific and energy-efficient heating by RF or microwaves in biological tissues.

4. Conclusions

In this manuscript, we report clear evidence of local differential heating enabled by pristine CNTs in a tissue phantom with similar dielectric properties to muscle. We used theoretical models to guide our optimization process of RF absorbers by maximizing their lengths and concentrations in a suspension. We experimentally verified this theoretical prediction of local differential heating with infrared thermography and numerical simulations. Given these results, pristine HiPCO CNTs are promising RF-absorbers for wireless local heat production while minimizing nonspecific heating in the tissue background. Looking forward, biocompatibility represents an important consideration for use of pristine CNTs. To ameliorate potential toxicity of CNTs, encapsulating CNTs into hydrogel or polymer networks may serve as a biocompatible approach that maintains the RF absorption of CNTs [22,23]. In future work, we plan to conduct studies on the biocompatibility of encapsulated CNT samples while validating their superior RF absorption for RFA and MH applications.

Acknowledgements

The authors thank Su Zhao for providing the HiPCO CNTs and Carl Keck for assistance with Raman spectroscopy. G.H. acknowledges two awards by NIH (5R00AG056636-04 and 1R34NS127103-01), a National Science Foundation (NSF) CAREER award (2045120), an NSF EAGER award (2217582), a Rita Allen Foundation Scholars Award, a Beckman Technology Development Grant, a grant from the Spinal Muscular Atrophy (SMA) Foundation, a grant from the Focused Ultrasound (FUS) Foundation, a gift from the Pinetops Foundation, two seed grants from the Wu Tsai Neurosciences Institute, and a seed grant from the Bio-X Initiative of Stanford University. N.J.R. gratefully acknowledges financial support from a Stanford Bio-X Honorary Graduate Student Fellowship and the NSF Graduate Research Fellowship Program. K.B. gratefully acknowledges financial support from the Knight-Hennessy Scholarship program and the U.S. Army LTHET program. Z.O. acknowledges the support by a Wu Tsai Neurosciences Institute Interdisciplinary Scholar Award. This material is based upon work supported by the National Science Foundation Graduate Research Fellowship Program under Grant No. DGE-1656518. Any opinions, findings, and conclusions or recommendations expressed in this material are those of the authors and do not necessarily reflect the views of the National Science Foundation. Part of this work was performed at the Stanford Nano Shared Facilities (SNSF), supported by the National Science Foundation under award ECCS-2026822.

Data availability statement

The data that support the findings of this study are available upon reasonable request from the authors.

Conflict of Interest Statement

The authors declare no conflict of interest.

Ethics Statement

This article does not contain any studies involving human or animal participants.

Table 1. Material properties used for FEM simulations.

Material	Density (kg/m³)	Specific heat (J/(kg K))	Thermal conductivity (W/(m K))	Dielectric function at 2 GHz
PBS	1,000	4,184	0.598	78.4 + 26.7i
Pristine CNT suspension in PBS	890	4,074	0.598	N/A

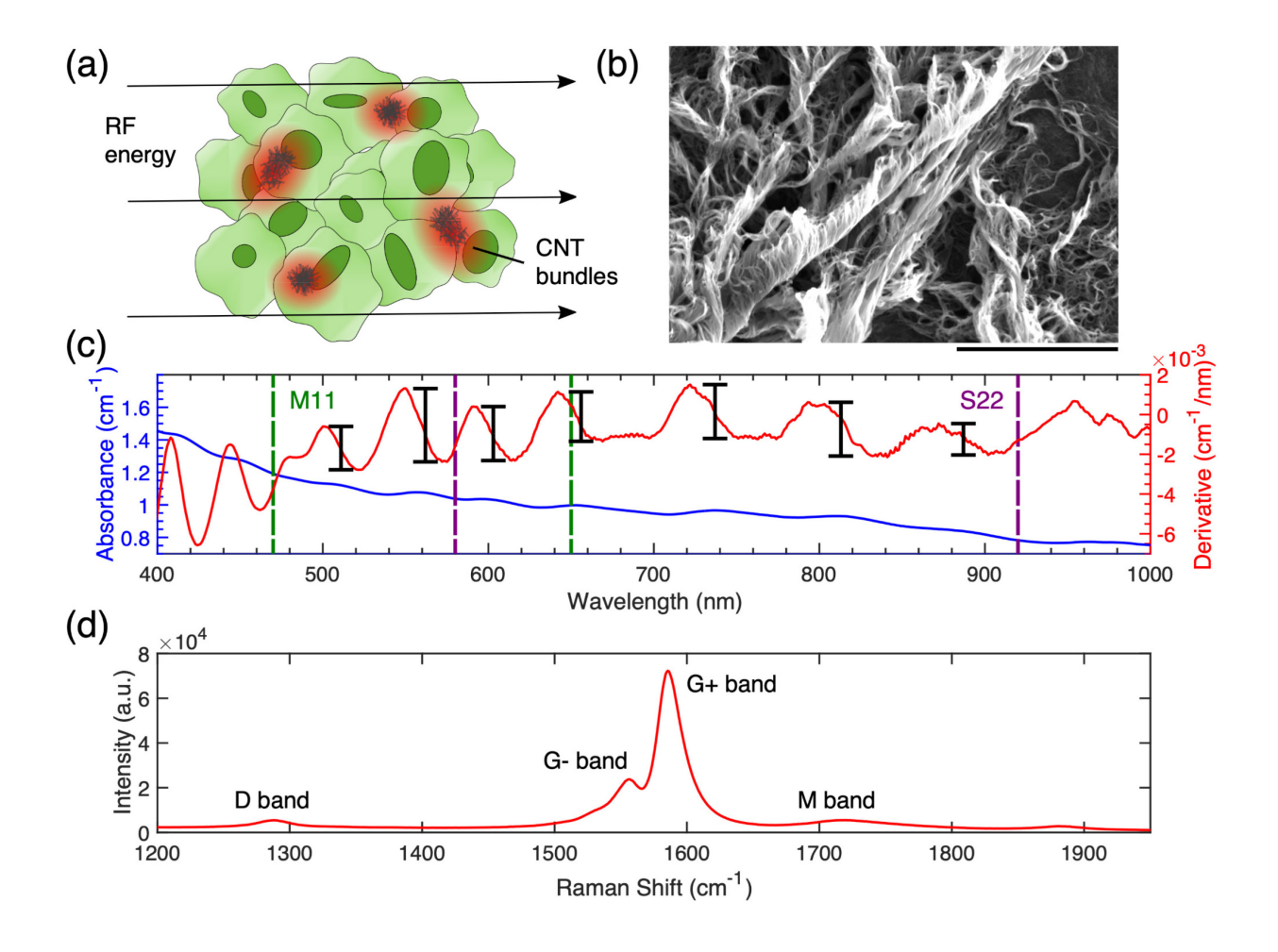


Figure 1. (a) Schematic of local differential heating of pristine CNTs in a soft tissue under RF irradiation. Region-specific differential heating is shown as red shades surrounding pristine CNTs. (b) Pristine CNTs imaged with a scanning electron microscope. Scale bar = 5 µm. (c) Absorbance spectrum of solubilized CNTs (left), and derivative of the absorbance (right). Green and purple dashed lines denote the M11 and S22 regions, respectively. Peaks marked with black bars fall within M11 or S22 and are included in calculations to determine the metallic vs. semiconducting ratio of the CNTs. (d) Raman spectrum of pristine CNTs showing the characteristic bands of CNTs.

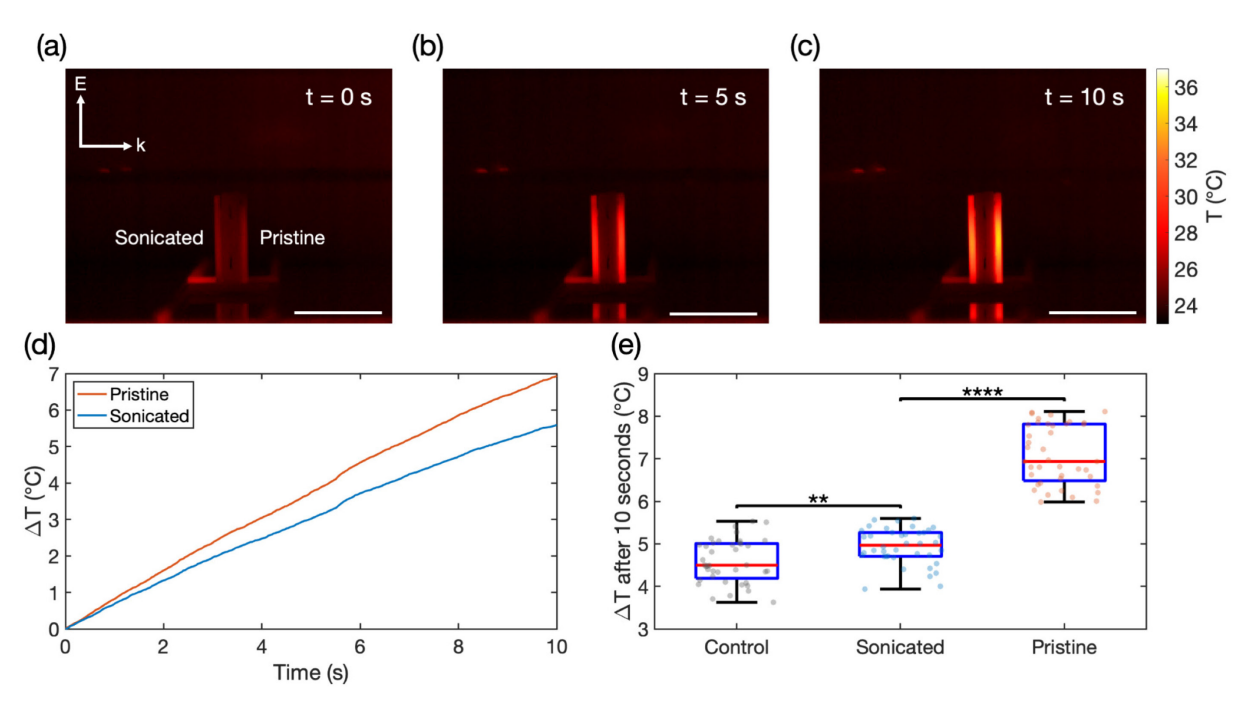


Figure 2. Thermal images of capillary tubes filled with sonicated (left) and pristine (right) CNTs at 0.5 mg/mL under RF irradiation at (a) t = 0 s, (b) t = 5 s, and (c) t = 10 s. Scale bars = 2 cm. (d) Representative traces of mean temperature vs. time for a pristine CNT capillary tube (red) and a sonicated CNT capillary tube (blue). (e) Box plot of the temperature increase after 10 s for control (20 mg/mL sodium deoxycholate), sonicated CNT, and pristine CNT capillary tubes, n = 40 trials each, ** p < 0.01, **** p < 0.0001.

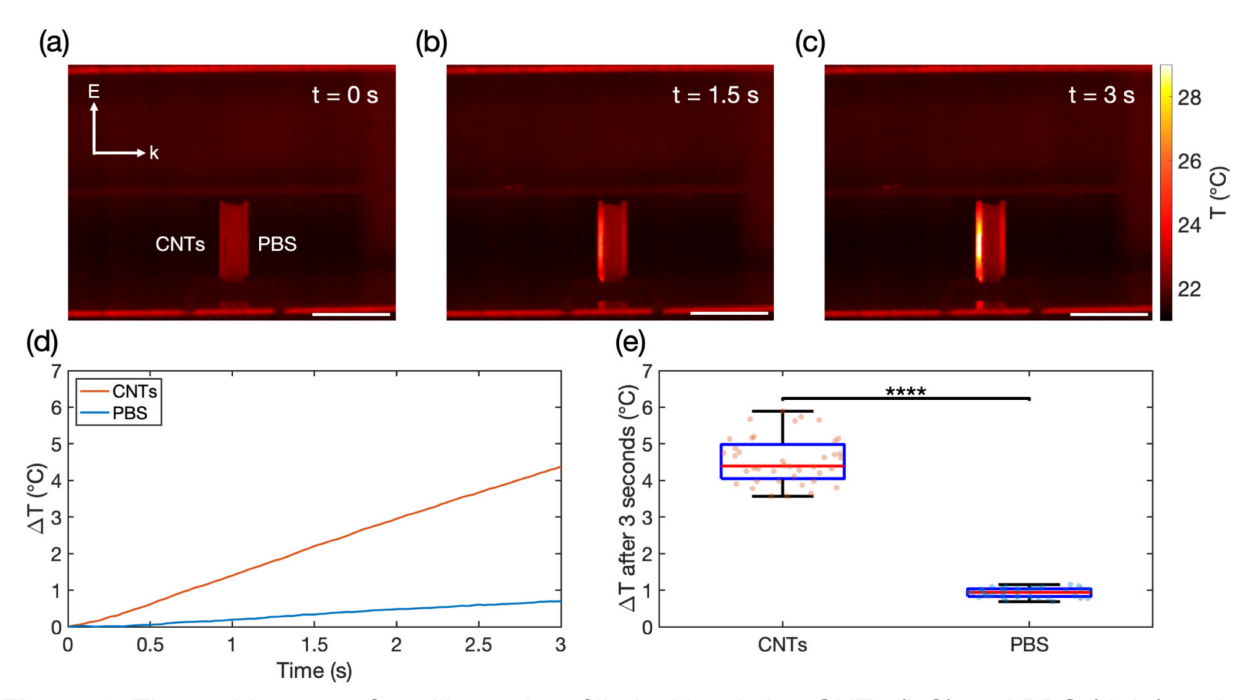


Figure 3. Thermal images of capillary tubes filled with pristine CNTs (left) and PBS (right) under RF irradiation at (a) t = 0 s, (b) t = 1.5 s, and (c) t = 3 s. Scale bars = 2 cm. (d) Representative traces of mean temperature vs. time for a PBS capillary tube (blue) and a pristine CNT capillary tube (red). (e) Box plot of ΔT after 3 s for PBS and pristine CNT capillary tubes, n = 40 trials each, **** p < 0.0001.

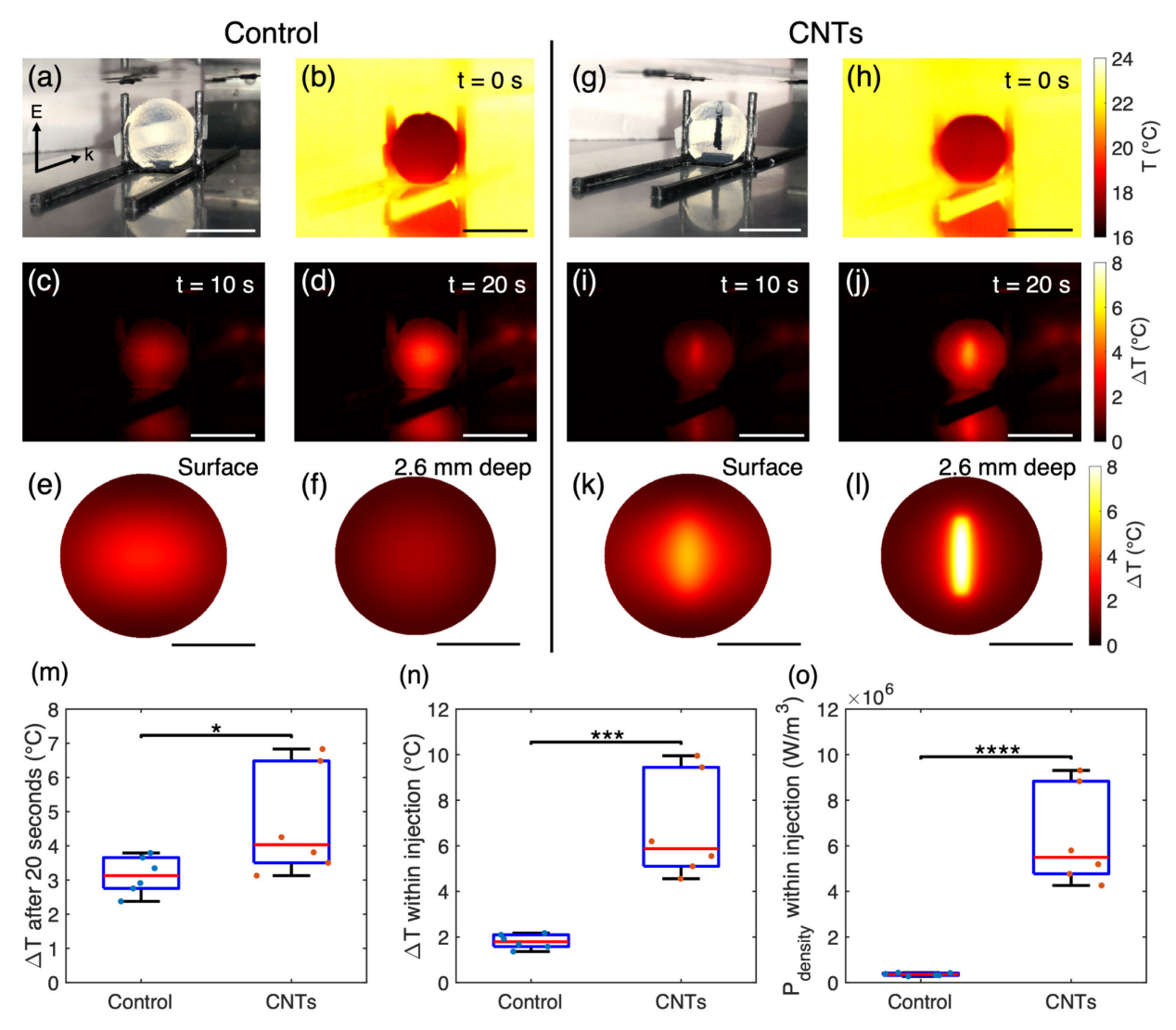


Figure 4. (a) Photograph of a control hemisphere, supported by a rack within the TEM cell. Scale bar = 2 cm. Thermal images of a control hemisphere under RF irradiation at (b) t = 0 s, (c) t = 10 s, and (d) t = 20 s. Scale bars = 2 cm. (e) FEM simulation of the temperature increase, ΔT , on the face of a control hydrogel after 20 s of RF irradiation. Scale bar = 1 cm. (f) FEM simulation of ΔT within a control hydrogel at 2.6 mm depth from its face after 20 s of RF irradiation. Scale bar = 1 cm. (g) Photograph of a CNT hemisphere, supported by a rack within the TEM cell. Scale bar = 2 cm. Thermal images of a CNT hemisphere under RF irradiation at (h) t = 0 s, (i) t = 10 s, and (j) t = 20 s. Scale bars = 2 cm. (k) FEM simulation of ΔT on the face of a CNT hydrogel after 20 s of RF irradiation. Scale bar = 1 cm. (I) FEM simulation of ΔT within the CNT hydrogel at 2.6 mm depth from its face after 20 s of RF irradiation. Scale bar = 1 cm. (m) Average surface ΔT after 20 s for the 6 control and 6 CNT hydrogels. The average was conducted over the circular ROIs shown in figure S1. (n) Extrapolated average ΔT over the cylindrical injection ROI after 20 s, based on COMSOL simulations (see Section 2.5 and Section 3). (o) Extrapolated power density averaged over the cylindrical injection ROI at 20 s, based on COMSOL simulations (see Section 2.5 and Section 3). Colorbars are consistent across each row. * p < 0.05, *** p < 0.001, **** p < 0.0001.

References

- [1] Han M, Chen L, Aras K, Liang C, Chen X, Zhao H, Li K, Faye N R, Sun B, Kim J-H, Bai W, Yang Q, Ma Y, Lu W, Song E, Baek J M, Lee Y, Liu C, Model J B, Yang G, Ghaffari R, Huang Y, Efimov I R and Rogers J A 2020 Catheter-integrated soft multilayer electronic arrays for multiplexed sensing and actuation during cardiac surgery *Nat. Biomed. Eng.* **4** 997–1009
- [2] Chu K F and Dupuy D E 2014 Thermal ablation of tumours: biological mechanisms and advances in therapy *Nat. Rev. Cancer* **14** 199–208
- [3] Rommelfanger N J, Ou Z, Keck C H C and Hong G 2021 Differential Heating of Metal Nanostructures at Radio Frequencies *Phys. Rev. Appl.* **15** 054007
- [4] Rommelfanger N J and Hong G 2021 On the feasibility of wireless radio frequency ablation using nanowire antennas *APL Mater.* **9** 071103
- [5] Lipomi D J, Vosgueritchian M, Tee B C-K, Hellstrom S L, Lee J A, Fox C H and Bao Z 2011 Skin-like pressure and strain sensors based on transparent elastic films of carbon nanotubes *Nat. Nanotechnol.* **6** 788–92
- [6] Zheng L X, O'Connell M J, Doorn S K, Liao X Z, Zhao Y H, Akhadov E A, Hoffbauer M A, Roop B J, Jia Q X, Dye R C, Peterson D E, Huang S M, Liu J and Zhu Y T 2004 Ultralong single-wall carbon nanotubes *Nat. Mater.* **3** 673–6
- [7] McEuen P L and Park J-Y 2004 Electron Transport in Single-Walled Carbon Nanotubes MRS Bull. 29 272–5
- [8] Shuba M V, Slepyan G Y, Maksimenko S A and Hanson G W 2010 Radiofrequency field absorption by carbon nanotubes embedded in a conductive host *J. Appl. Phys.* **108** 114302
- [9] Gannon C J, Cherukuri P, Yakobson B I, Cognet L, Kanzius J S, Kittrell C, Weisman R B, Pasquali M, Schmidt H K, Smalley R E and Curley S A 2007 Carbon nanotube-enhanced thermal destruction of cancer cells in a noninvasive radiofrequency field *Cancer* 110 2654– 65
- [10] Beckler B, Cowan A, Farrar N, Murawski A, Robinson A, Diamanduros A, Scarpinato K, Sittaramane V and Quirino R L 2018 Microwave Heating of Antibody-functionalized Carbon Nanotubes as a Feasible Cancer Treatment *Biomed. Phys. Eng. Express* 4 045025
- [11] Chall A, Stagg J, Mixson A, Gato E, Quirino R L and Sittaramane V 2021 Ablation of cells in mice using antibody-functionalized multiwalled carbon nanotubes (Ab-MWCNTs) in combination with microwaves *Nanotechnology* 32 195102
- [12] Davis H C, Kang S, Lee J-H, Shin T-H, Putterman H, Cheon J and Shapiro M G 2020 Nanoscale Heat Transfer from Magnetic Nanoparticles and Ferritin in an Alternating Magnetic Field *Biophys. J.* 118 1502–10
- [13] Arnold M S, Green A A, Hulvat J F, Stupp S I and Hersam M C 2006 Sorting carbon nanotubes by electronic structure using density differentiation *Nat. Nanotechnol.* **1** 60–5
- [14] Huang L, Zhang H, Wu B, Liu Y, Wei D, Chen J, Xue Y, Yu G, Kajiura H and Li Y 2010 A

- Generalized Method for Evaluating the Metallic-to-Semiconducting Ratio of Separated Single-Walled Carbon Nanotubes by UV-vis-NIR Characterization *J. Phys. Chem. C* **114** 12095–8
- [15] Bakhshiani M, Suster M A and Mohseni P 2015 A 9 MHz-2.4 GHz Fully Integrated Transceiver IC for a Microfluidic-CMOS Platform Dedicated to Miniaturized Dielectric Spectroscopy *IEEE Trans. Biomed. Circuits Syst.* **9** 849–61
- [16] Hone J, Batlogg B, Benes Z, Johnson A T and Fischer J E 2000 Quantized phonon spectrum of single-wall carbon nanotubes *Science* **289** 1730–3
- [17] Welsher K, Liu Z, Sherlock S P, Robinson J T, Chen Z, Daranciang D and Dai H 2009 A route to brightly fluorescent carbon nanotubes for near-infrared imaging in mice *Nat. Nanotechnol.* 4 773–80
- [18] Jorio A and Saito R 2021 Raman spectroscopy for carbon nanotube applications *J. Appl. Phys.* **129** 021102
- [19] M.M. Paulides, H. Dobsicek Trefna, S. Curto, and D.B. Rodrigues 2020 Recent technological advancements in radio frequency- and microwave-mediated hyperthermia for enhancing drug delivery *Adv. Drug Deliv. Rev.* **163-164** 3–18
- [20] Vichchulada P, Cauble M A, Abdi E A, Obi E I, Zhang Q and Lay M D 2010 Sonication Power for Length Control of Single-Walled Carbon Nanotubes in Aqueous Suspensions Used for 2-Dimensional Network Formation *J. Phys. Chem. C* **114** 12490–5
- [21] Gabriel S, Lau R W and Gabriel C 1996 The dielectric properties of biological tissues: II. Measurements in the frequency range 10 Hz to 20 GHz *Phys. Med. Biol.* **41** 2251–69
- [22] Ahadian S, Ramón-Azcón J, Estili M, Liang X, Ostrovidov S, Shiku H, Ramalingam M, Nakajima K, Sakka Y, Bae H, Matsue T and Khademhosseini A 2014 Hybrid hydrogels containing vertically aligned carbon nanotubes with anisotropic electrical conductivity for muscle myofiber fabrication *Sci. Rep.* **4** 4271
- [23] Singh N, Chen J, Koziol K K, Hallam K R, Janas D, Patil A J, Strachan A, G Hanley J and Rahatekar S S 2016 Chitin and carbon nanotube composites as biocompatible scaffolds for neuron growth *Nanoscale* **8** 8288–99